High-Resolution Real-time FBG Interrogation System using a Gain-Switched Dual Optical Frequency Comb

This article has been accepted for publication in Journal of Lightwave Technology. This is the author's version which has not been fully edited and content may change prior to final publication. Citation information: DOI 10.1109/JLT.2026.3705621

High-Resolution Real-time FBG Interrogation System using a Gain-Switched Dual Optical Frequency Comb

Minghao Wei, Conor McArdle, Alejandro Rosado, Malhar A. Nagar, Davide Janner, and Prince M. Anandarajah, *Senior Member, IEEE*

***Abstract*—We demonstrate a compact, low-cost fibre Bragg grating interrogation system combining an externally injected gain-switched dual optical frequency comb with embedded real-time processing that achieves 0.6 pm resolution at 1011 Hz interrogation rates and <75 fm resolution at measurement rates below 3Hz. The system employs optical heterodyning and receiver integrated curve fitting algorithms to enable real-time operation. Comprehensive characterization of dual-comb stability, receiver processing performance, and algorithm accuracy validates the system's capabilities and identifies wavelength-dependent resolution behaviour linked to variations in comb-line signal-to-noise ratio. The demonstrated resolution-speed trade-off and femtometre-scale measurement capability establish this architecture to be well-suited for high-sensitivity, fast-response sensing applications.**

***Index Terms*— Fibre Bragg gratings, Dual optical frequency comb, High resolution interrogation system, Real-time processing, Gain switching.**

I. INTRODUCTION

Fibre Bragg gratings (FBGs) were first demonstrated in 1978 by Ken Hill [1]. Since then, they have been widely used in optical sensing across various fields, such as biochemical sensing [2], aerospace engineering [3], and structural monitoring [4]. Most of these applications rely on tracking parameters such as temperature [3], [5], pressure [6] and strain [7]. When an FBG experiences axial strain and/or a temperature change, either directly or via transduction of other measurands into strain/temperature, the Bragg wavelength shifts in a predictable manner that is typically well-approximated as linear over moderate ranges, with practical measurements often requiring consideration of strain-temperature cross-sensitivity and packaging effects [8]. Its widespread adoption can be attributed to low cost, lightweight construction, real-time response, high accuracy and sensitivity, and immunity to electromagnetic interference.

Several interrogation methods have been developed to extract the Bragg wavelength shift in FBGs, induced by external perturbations (e.g., strain, temperature, etc.). One common approach uses a broadband light source together with an optical spectrum analyser (OSA) [5], [9], to monitor the reflected spectrum. While this method is widely used for laboratory characterisation because of its simplicity and direct spectral visibility, it typically suffers from limited acquisition speed, bulky instrumentation, poor signal to noise ratio (SNR), and high cost. Another widely used method entails sweeping the wavelength of a tunable laser (TL) across the FBG spectral profile. The reflected/transmitted signal is then received by a photodiode (PD), and the detected power is mapped to wavelength [10], [11], [12]. This approach can achieve large dynamic ranges (>3 nm, i.e., approximately 3000 με), but typically with wavelength resolutions at the picometre (pm) level [13]. In addition, as the FBG spectrum must be reconstructed through wavelength scanning rather than single-shot acquisition, achieving high accuracy and long-term stability typically relies on careful control of the laser sweep (e.g., linearization) and robust wavelength calibration, often with tight timing alignment between the scan and the calibration reference.

To address such concerns, dual optical frequency combs (DOFCs) have been employed [14], [15], [16] for the interrogation of FBGs. Owing to their multi-wavelength nature, the DOFC enables single-shot interrogation of the FBG without wavelength scanning [17]. The DOFC approach uses two optical frequency combs with slightly different free spectral ranges (FSRs). In practice, one comb line (tone) from each optical frequency comb (OFC) is aligned to act as a common wavelength reference, such that the two combs share a mutual optical anchor. Subsequently, these two combs are combined and photodetected, producing a radio-frequency (RF) comb through the process of heterodyne detection, effectively down-converting the optical spectra into low RF frequencies, which eventually maps the optical spectral information into the RF domain. This frequency down-conversion eliminates the need for a high-resolution OSA and avoids wavelength scanning, thereby reducing system complexity and enabling real-time interrogation using mature,

This work Research conducted with the financial support in part by the Taighde Éireann – Research Ireland under Grant number 13/RC/2077_P2 at CONNECT: the Research Ireland Centre for Future Networks and NATO SPS.MYP.G6056. *(Corresponding author:* Minghao Wei*).* First author Minghao Wei, Conor McArdle, Alejandro Rosado, and Prince M. Anandarajah are with the Photonics Systems and Sensing Lab (PSSL), School of Electronic Engineering, Dublin City University, Glasnevin, Dublin 9, Ireland (e-mail: minghao.wei2@mail.dcu.ie; conor.mcardle@dcu.ie; alejandro.rosado@dcu.ie; prince.anandarajah@dcu.ie). Malhar A. Nagar and Davide Janner are with the Dipartimento di Scienza Applicata e Tecnologia (DISAT), Politecnico di Torino, Corso Duca degli Abruzzi, 24, 10129, Turin, Italy (e-mail: malhar.nagar@polito.it; davide.janner@polito.it). Color versions of one or more of the figures in this article are available online at http://ieeexplore.ieee.org.

This article has been accepted for publication in Journal of Lightwave Technology. This is the author's version which has not been fully edited and content may change prior to final publication. Citation information: DOI 10.1109/JLT.2026.3705621

low-cost RF electronics [17].

DOFC-based FBG interrogation has been demonstrated using various dual-comb generation schemes, including Yb- [15] and Er-doped [18] fibre mode-locked lasers (MLLs), and electro-optic modulators (EOMs) [16]. MLL-based DOFCs can provide broadband comb spectra [19]. However, their FSR is determined by the laser cavity length. In semiconductor MLLs, the cavity length is fixed, thereby limiting FSR tunability. In contrast, fibre MLLs have cavity lengths that are more sensitive to environmental perturbations, requiring additional stabilisation mechanisms. EOM-based DOFC generation offers excellent FSR tunability [14], but typically requires cascaded modulators that introduce insertion loss and result in greater system complexity due to the need for active stabilization (bias drift). Externally injected gain-switched laser (EI-GSL) based DOFC generation is known for its simplicity, robustness, cost-effectiveness, suitability for photonic integration, and flexible tunability in both FSR and wavelength [20], [21], [22]. Although this technique typically generates OFCs with relatively narrow bandwidths, the generated comb lines generally exhibit higher power and previous EI-GSL DOFC based FBG interrogation have demonstrated dynamic ranges of several hundreds to ~1300 με [22], comparable to some MLL-based interrogators [18], [19].

In this work, we present an FBG interrogation system implemented using an EI-GSL based DOFC interrogator in conjunction with a purpose-built processing unit as the receiver. This receiver comprises an analog-to-digital converter (ADC) and a microcontroller unit (MCU), enabling the enhancement of previous demonstrations on dual-comb FBG interrogation [7], [24] by achieving real-time fm level sensing. Specifically, by using the proposed low-cost real-time FBG interrogation system, a static measurement resolution of ~0.6 pm was experimentally demonstrated at an interrogation rate of 1,011 Hz. This clearly surpasses previously reported results, such as 5 pm [15], 1.7 pm [25] and 0.855 pm [24], all of which used off-line processing. We attribute the improved resolution in this work to two main enhancements. First, both OFC sources were characterised and optimised according to an OFC figure of merit (FoM), as defined in [26], to enhance comb quality while reducing the resulting RF amplitude fluctuations. Second, a simulation-driven comparison of several curve fitting algorithms was performed. The results from such analysis allowed us to identify a processing method that yielded a higher resolution and lower systematic error, subsequently implemented on the embedded receiver. The fitting strategy we adopt maintains accuracy across various FBG profiles. In contrast, while the X-dB bandwidth method [27] and Gaussian-based estimators [28] used in other DOFC interrogation [7] systems are effective for near-symmetric FBG spectra, their performance can become more sensitive to spectral asymmetry. It is also important to note that the resolution can be further improved by increasing the discrete Fourier transform (DFT) averaging factor, albeit at the expense of the interrogation rate. The best resolution achieved in this study was ~36 fm at an interrogation rate of 2.27 Hz, surpassing previous work, which achieved ~224 fm [7] and ~190 fm [23] using offline processing. This trade-off between rate and resolution has been experimentally demonstrated, and the results also revealed a wavelength dependence of the measurement resolution.

This paper is organized as follows: Section II.A describes the detailed implementation and operating parameters of the DOFC interrogator. Section II.B presents the design of the receiver, including the signal processing pipeline and processing time. Section III presents the characterisation and optimisation of the DOFC, including stability measurements of the optimized combs, which are critical to achieving the high resolution demonstrated in this work. Section IV details the receiver software implementation, where different RF-comb envelope curve fitting algorithms are simulated and compared. Finally, Section V presents the static interrogation experiments across multiple Bragg wavelengths, demonstrating the trade-off between interrogation rate and resolution and revealing the wavelength dependence of achievable resolution.

II. Experimental Setup

The interrogation system used in this work, as illustrated in **Fig. 1**, comprises a DOFC and a receiver containing a photodetector (PD) and a custom real-time processing platform. A commercial FBG is used as the device under test (DUT). Each of these elements is described, in more detail, below.

A. EI gain-switched DOFC interrogator setup

The DOFC interrogator is presented in **Fig. 1 (a).** It has three semiconductor lasers in a primary-secondary configuration. A narrow linewidth (~10 kHz) wavelength tunable (C-band) semiconductor laser is used as the primary source (PurePhotonics PPCL550). Meanwhile, two Fabry-Perot (FP) lasers housed in a 7-pin temperature-controlled butterfly package with an RF connector for direct modulation are used as the secondary sources (Eblana Photonics EP1550-0-FP-H19-FM).

Both FPs are gain-switched [29] using sine waves, amplified to ~24 dBm, at frequencies of 1 and 0.99998 GHz, respectively, resulting in a ΔFSR of 20 kHz. The EI-GSL architecture also provides flexible FSR tunability, where a smaller FSR provides more sampling points across the FBG profile, potentially improving the achievable interrogation resolution. However, this may degrade the comb quality, including poorer spectral flatness and reduced comb-line SNR [30], which can limit the interrogation range and resolution.

The individual gain-switched OFCs are mutually injection locked using the TL acting as a common primary laser providing phase synchronisation between both secondary lasers. The resulting OFCs are then heterodyned on a low bandwidth PD, which down-converts the optical signal into an RF comb with a tone spacing equal to the ΔFSR. In FBG interrogation, this enables the reconstruction of FBG features into RF frequencies, easily measurable with low-frequency electronics.

This article has been accepted for publication in Journal of Lightwave Technology. This is the author's version which has not been fully edited and content may change prior to final publication. Citation information: DOI 10.1109/JLT.2026.3705621

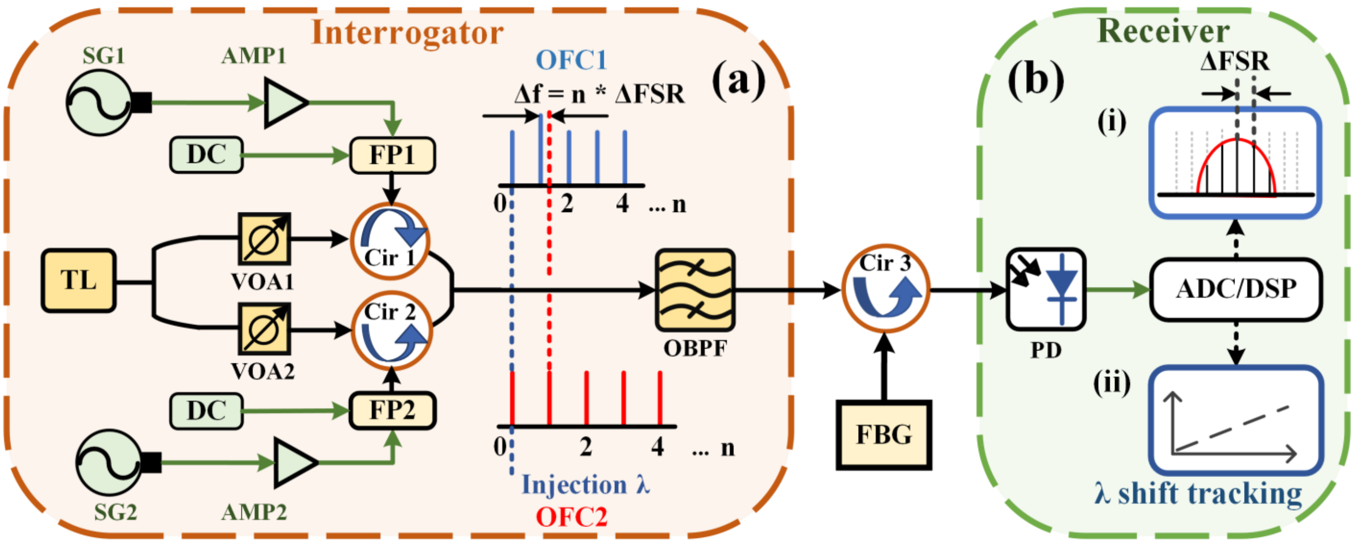

Fig. 1. Experimental setup of the FBG interrogation system consisting of **(a)** the EI-GSL-based DOFC interrogator and **(b)** the real-time receiver. TL: tunable laser; VOA: variable optical attenuator; Cir: optical circulator; FP: Fabry-Perot laser; AMP: RF amplifier; SG: RF signal generator; OBPF: optical bandpass filter; FBG: fibre Bragg grating; PD: photodetector.

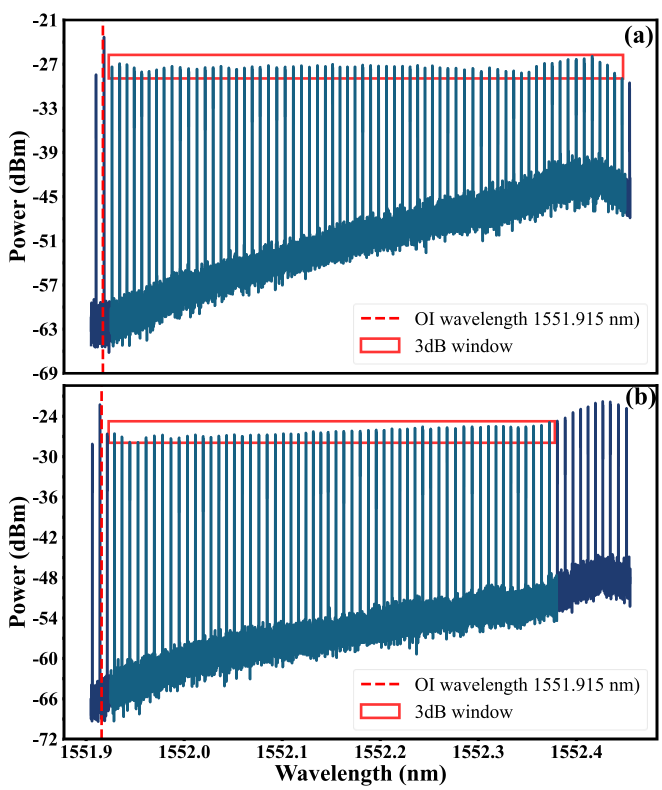

Fig. 2. A close-up view of the optical spectra of the generated OFCs. **(a)** OFC 1 with the 3-dB window ranging from 1551.920 nm to 1552.455 nm and **(b)** OFC 2 with the 3-dB window ranging from 1551.920 nm to 1552.350 nm.

The wavelength of the primary laser is set to 1551.915 nm and injected into the gain-switched FPs via a 1 by 2 passive splitter, variable optical attenuators (VOAs) and circulators. This injection wavelength serves as the reference wavelength and is indicated in **Fig. 1 (a)** by a blue dotted line. This pair of comb lines is designated index 0 in each comb. The average power injected into FP 1 and FP 2 is –16.27 dBm and –14.97 dBm, respectively.

The optical spectra (using a high resolution OSA - APEX AP2083A with a resolution of 0.16 pm (20 MHz)) of the resulting OFCs, at port 3 of their respective optical circulators (1 and 2), are shown in **Fig. 2 (a)** and **(b)**.

The two OFCs are then combined via a 50:50 optical coupler and passed through a wavelength (1525–1610 nm) and bandwidth (50–950 pm) tunable optical bandpass filter (OBPF) (EXFO XTM-50). It is important to note that all individual fibres and components used in this experiment prior to the OBPF are polarisation maintaining, which contributes to mitigating the random fluctuations of the power in the fibre. The filter suppresses the injected and shorter wavelength comb lines, thus removing duplicated heterodyned tones in the subsequently generated RF comb [22]. For comb lines at wavelengths longer than the injection wavelength, the filter is set to select only those within a 3-dB spectral window. The selection of the spectrally flat portion of the DOFC for interrogation reduces errors caused by amplitude unevenness.

B. Fibre Bragg grating

The DUT used in this work is a commercially available Gaussian-apodized uniform FBG (AOS GmbH) that has a full width half maximum (FWHM) of 0.176 nm and a reflectivity of 99%. It incorporates an integrated stepper motor that mechanically stretches the grating to apply strain. Although this FBG includes a built-in temperature control circuit that compensates for thermal drift by adjusting the motor position, this function was intentionally disabled during the experiment. This ensured that the measured Bragg wavelength shifts resulted solely from the programmed motor steps, and that the temperature-compensation mechanism did not introduce additional uncertainty into the interrogation measurements. The FBG was further insulated with polystyrene foam to minimise environmental temperature variations.

This article has been accepted for publication in Journal of Lightwave Technology. This is the author's version which has not been fully edited and content may change prior to final publication. Citation information: DOI 10.1109/JLT.2026.3705621

C. Real-time receiver

The reflected output from the FBG (port 3 of circulator 3) is fed into a low-cost, custom-built receiver (as illustrated in **Fig. 1 (b)**). A PD (PDA10D, 15 MHz bandwidth) converts the reflected optical signal into an electrical waveform. This electrical signal is then fed into the real-time processing platform consisting of an ADC and a MCU. The unit is constructed on a single custom-designed printed circuit board (PCB), comprising an AC-coupled 50 Ω analog input followed by a low-distortion buffer integrated circuit (IC) (LTC6409) with a 10 GHz bandwidth. The buffered signal then passes through a fifth-order 5 MHz low-pass analog anti-aliasing filter with a passband ripple of less than ±0.1 dB. This frontend drives the balanced input of the ADC IC (ADC14L029), which has a dedicated low-jitter 10 MHz sampling clock. The 14-bit ADC's parallel digital output connects to the MCU (i.MXRT1060 600 MHz ARM Cortex M7), which receives a copy of the clock signal for sample-read synchronization at the 10 MHz sample rate. This dedicated low-cost processing unit, combined with the low-cost (<€10k estimated from bill of materials to build a lab. prototype) EI-GSL-based DOFC interrogator, enables a real-time and cost-effective FBG interrogation system.

The PCB layout design and on-board USB power supply conditioning/regulation ensure a low system noise floor, matching the published ADC specification of 74 dBc SNR, which is substantially below the noise floor of the PD input signal. The unit may be configured for a number of samples (N) from 1024 up to 16384 samples and DFT averaging up to 1000 DFTs per average. This allows the centre frequency (CF) measurement rate to be balanced against measurement noise, by way of controlling digitisation processing gain and DFT noise power.

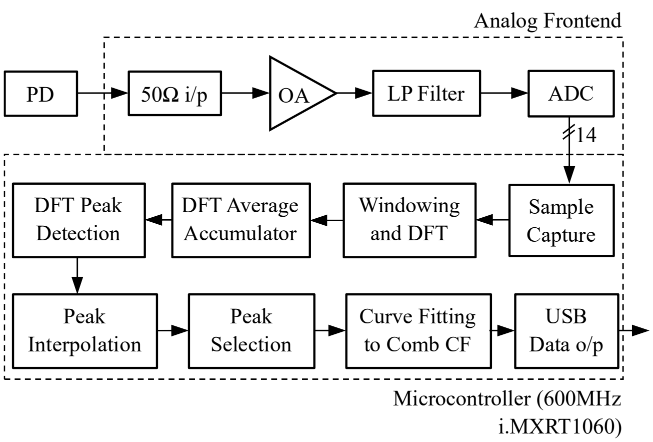

Fig. 3. Hardware and software processing pipeline of the real-time ADC/DSP unit. PD: photodiode, OA: operational amplifier, LP filter: low-pass filter, ADC: analog-to-digital converter, DFT: discrete Fourier transform.

The MCU runs the complete digital signal processing (DSP) chain, as illustrated by **Fig. 3**, which shows a schematic representation of the ADC/DSP processing pipeline.

This process entails sample capture, windowing and DFT magnitude computation, followed by DFT averaging to reduce frequency-domain noise. Peaks are then detected using a 4-point DFT moving window, interpolated for high-accuracy magnitude and frequency (based on methods in [31]), and then fitted by curve fitting algorithms to estimate the RF-comb CF. The MCU also manages a high-speed USB serial interface for real-time output and configuration. It can stream DFT frames, interpolated peak data, curve-fit results, and execution metrics to a PC at rates up to ~1800 RF CF measurements per second, depending on sample length and averaging settings. **Fig. 4** shows the sample capture and processing times for a single CF measurement cycle across different sample lengths, without DFT averaging. Additional DSP computation time includes all additional operations required to produce a final CF measurement: sample windowing, DFT peak detection and interpolation, and curve fitting estimation of the CF. When DFT averaging is used, sample capture times and fast Fourier Transform (FFT) execution times will be multiplied by the number of DFTs that are averaged per measurement. All additional processing is done once, regardless of the number of DFTs being averaged.

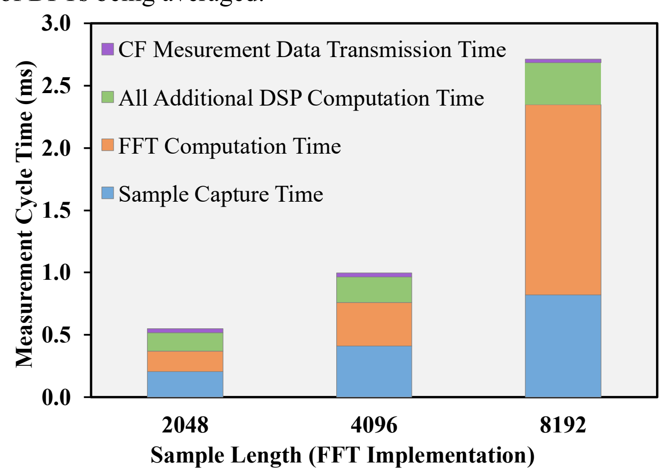

Fig. 4. Cumulative/total processing times for the CF measurement process, with no DFT averaging. Not shown in figure, 16384 FFT yields a total CF measurement processing time of ~9.3 ms, of which the sample capture time accounts for 1.638 ms, FFT computation time accounts for 7.030 ms, and all Additional DSP Computation Time accounts for 0.579 ms. CF: centre frequency, DFT: discrete Fourier transform, FFT: fast Fourier transform.

The sample length and number of DFT averaging will impact the resolution of the CF measurement, as well as determine the measurement rate. Using an optimised FFT algorithm with pre-computed phase-factors stored in memory, the DFT can be computed efficiently by the MCU for sample lengths of 4096, or less. For longer sample lengths, there is insufficient memory to pre-compute all FFT phase-factors and a significantly less efficient, staged FFT computation is required. In any case, a sample length of 4096 has been found to reliably detect RF peak comb lines spaced 20 kHz apart; this sample length provides approximately 8 DFT points per comb line. Additionally, the 3 dB reduction in noise power gained by doubling the sample length, can instead be gained by doubling the number of DFT samples, at less

This article has been accepted for publication in Journal of Lightwave Technology. This is the author's version which has not been fully edited and content may change prior to final publication. Citation information: DOI 10.1109/JLT.2026.3705621

computational expense. Therefore, we settle on a sample length of 4096 (DFT length of 2048) for all measurements. The number of DFT averaging may then be chosen to balance measurement rate and measurement resolution. With no DFT averaging, the total CF processing time is approximately 0.996 ms, corresponding to a constant measurement rate of approximately 1011 Hz. Within this processing time, sample capture and FFT computation account for more than 75% of the total CF measurement cycle time, as shown in **Fig. 4**. Although the interrogation speed could be further improved using higher-speed hardware or more optimised DSP implementations, this would increase the system cost and complexity. Alternatively, reducing the sample length would decrease both acquisition and FFT computation time, but at the expense of frequency-domain resolution and RF-comb peak localisation accuracy. With 100× DFT averaging, the maximum measurement rate drops to approximately 13 Hz. The measurement rate is approximately proportional to $1/n_{avg}$, n_{avg} being the DFT averaging factor, whereas the statistical effect of averaging will reduce measurement standard deviation by a factor of the order of $1/\sqrt{n_{avg}}$. Therefore, there is a point of diminishing returns in applying DFT averaging, as the improvement in measurement resolution becomes progressively smaller while the interrogation rate continues to decrease. Ultimately, achieving both high-rate and high-resolution measurements requires low noise in the optical and receiver domains rather than excessive digital averaging.

III. Characterisation and Optimisation of the OFC

As it is well known, each RF comb line is generated by heterodyning a pair of optical comb lines. Hence, the amplitude fluctuations in the optical domain translate directly into amplitude fluctuations in the electrical domain (RF comb). As the RF comb is subsequently used for curve fitting to extract the CF, amplitude instabilities in the RF domain directly limit the resolution of CF estimation. This, in turn, degrades the overall interrogation accuracy and resolution, regardless of the fitting algorithm employed. Therefore, a detailed analysis of the amplitude stability of the OFCs is essential to evaluate and optimise the interrogator performance.

By optimising the modulation amplitude, TL wavelength and power, FP laser DC bias, and operating temperature of the FP lasers, flat-top OFCs were generated. During the OFC optimisation process, a FoM was used to evaluate the trade-off between the achievable comb spectral width and the average comb-line SNR, allowing the selection of operating conditions that balance spectral coverage and comb-line quality. OFC1 and 2 exhibited an overlapping 3-dB spectral window ranging from 1551.920 nm to 1552.350 nm, with side-mode suppression ratios (SMSRs) [32] of 26.23 dB and 26.10 dB, respectively. The corresponding average SNR, computed across all individual comb lines within the 3 dB window, was measured to be 22.88 dB and 28.53 dB.

The amplitude stability characterisation was carried out by capturing the optical spectrum of each OFC, once every 6 seconds, over a 30-minute time frame. 54 comb lines from each OFC, all in a common 3 dB spectral window, were chosen for this amplitude stability test. The data obtained was then analysed in terms of the temporal evolution of the amplitude of each tone by means of its mean value, standard deviation and maximum deviation with respect to the mean value. The corresponding results from this analysis are depicted in **Fig. 5**.

The results show that for OFC 1, the maximum fluctuation is 0.69 dB, with an average fluctuation of 0.52 dB across the chosen lines. In the case of OFC 2, the maximum fluctuation is 0.83 dB, with an average of 0.59 dB across the chosen range. Although OFCs optimization can significantly reduce amplitude fluctuations, residual fluctuations cannot be completely eliminated in practice. Consequently, the remaining amplitude instability represents one of the fundamental factors limiting the ultimately achievable interrogation resolution.

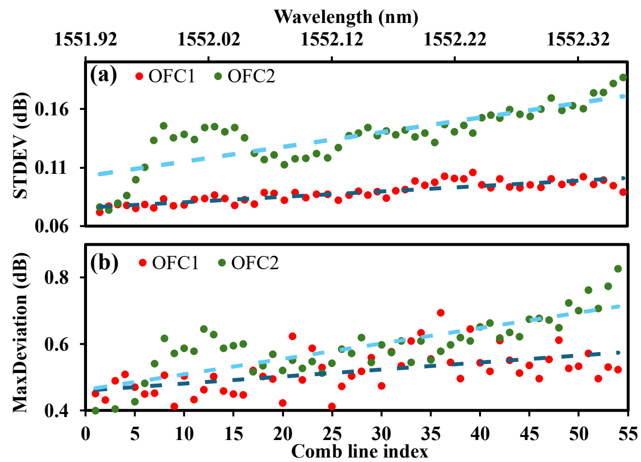

Fig. 5. OFCs stability test results, **(a)** standard deviation of the amplitude fluctuations of OFCs, and **(b)** maximum amplitude deviation of OFCs.

Fig. 5 (a) plots the standard deviation of each comb line amplitude measured over the 30 minutes, with the bottom x-axis corresponding to the comb line index and the top x-axis showcasing the corresponding optical wavelength. The data show a clear upward trend: as the comb line index increases (corresponding to longer optical wavelengths), the standard deviation increases. **Fig. 5 (b)** presents the peak-to-peak amplitude deviation, defined as the difference between the maximum and minimum recorded amplitude for each comb line, and exhibits the same behaviour. These results illustrate the effect of the locality of the external injection. In essence, the tones that are located further away from the injection wavelength exhibit higher amplitude fluctuations. This effect can be attributed to the reduction in SNR of the comb lines at longer wavelengths (further from the injection wavelength) [32], as shown in **Fig. 2**. Consequently, based on the observed OFCs stability characteristics, it can be anticipated that the achievable resolution depends on the spectral position of the Bragg wavelength relative to the spectral output of the DOFC.

This article has been accepted for publication in Journal of Lightwave Technology. This is the author's version which has not been fully edited and content may change prior to final publication. Citation information: DOI 10.1109/JLT.2026.3705621

Specifically, when the Bragg wavelength shifts toward longer optical wavelengths (further from the injection wavelength) with increasing measurand, the increased amplitude fluctuations are expected to reduce the achievable resolution. This characteristic is experimentally verified by the static interrogation results presented in Section V.

Shifting the injection wavelength toward the centre of the OFC spectrum, results in an increase in the SMSR, which in turn could reduce the amplitude fluctuations [32]. However, injection into the centre of the OFC results in a narrower (Gaussian shaped) OFC. Hence, a trade-off exists between SMSR and the width/flatness of the OFC [30]. It is important to note that the flat spectral region directly determines the effective interrogation range of the FBG sensor.

IV. RF COMB AND CURVE FITTING

After the characterisation and optimisation of the amplitude stability of the DOFC, it was then employed to interrogate the FBG and also used for the simulation and optimisation of the curve fitting algorithms. The receiver down-converts the reflected DOFC into an RF comb and performs curve fitting to track the RF-comb centre frequencies, which directly map to Bragg-wavelength shifts.

A. RF comb

As described above, the OBPF transmits only those DOFC comb lines that fall within the 3 dB window. In a back-to-back configuration (without the FBG) of the interrogation system, the optical lines heterodyned on the PD were down converted to a spectrally flat RF comb with a tone spacing (F_{ls}) of 20 kHz, as shown in **Fig. 6 (a)**. 58 RF comb lines exceeded a threshold power level of -60 dBm and 54 of these tones lay within a 3 dB spectral window, corresponding to an interrogation range of ~434.2 pm. The red dots in the figure are the detected RF tone peaks interpolated in frequency and magnitude, which are computed and outputted by the ADC/DSP unit.

Subsequently, when the system is applied towards the interrogation of the FBG, only those comb lines that fall within the FBG reflection profile are reflected to the receiver and down converted to an RF comb, as illustrated in **Fig. 6 (b)**. The Bragg wavelength was set to 1552.312 nm, which corresponded to the upper limit of the interrogation range.

B. Curve fitting algorithm for the reflected RF comb

RF tones peak detection followed by curve fitting was initially used to extract the Bragg wavelength from the RF comb. The curve fitting and CF (f_c) estimation method is a combination of two least-squares curve fitting methods, referred to as *Quad* and *DualPoly4*. Additional methods such as *Poly4OptCF* and *CubicSpline*, were also employed mainly for benchmarking. Apart from the Quad method, all others were fit to log-magnitude data. The peak points used for curve fitting are selected from the detected DFT spectral peaks based on an amplitude windowing criterion. As illustrated in **Fig. 6 (b)**, the peak-selection window is defined relative to the maximum magnitude p_{max}, with the lower and upper bounds W_{min} and W_{max} specified as power offsets (in dB) from p_{max}. Only those DFT spectral peaks whose magnitudes fall within this window are retained as fitting points. A brief description of each of the methods is provided below.

- Quadratic Least Squares (*Quad*) method: The vertical parabola $m(f) = af^2 + bf + c$ is least squares fitted to the selected profile points, magnitude (voltage) values. The estimated centre frequency, f_c^*, is the x-coordinate of the vertex of the resulting parabola, $f_c^* = -b/2a$ [24].
- Symmetric fourth order polynomial fit (*Poly4OptCF*): The symmetric bicubic polynomial $m(f) = a_0 + a_2(f - f_c)^2 + a_4(f - f_c)^4$ is least squares fitted to the selected profile points. The secant method is then applied to search for the optimal f_c^* such that the total square error of the polynomial curve fit is minimised. The aim of using a symmetric higher order polynomial is to enable a closer fit to the data while avoiding the possibility of overfitting with too many free parameters. As with the *Quad* method, inaccuracies are expected due to the FBG profile not being symmetric.
- The dual fourth order polynomial fit method (*DualPoly4*): This method splits the selected points left and right of the centre point and separately fits a bicubic polynomial to each subset (as shown in **Fig. 6 (b)**). An initial CF estimate is obtained using the *Quad* method. This CF estimate is used to split the points set and is also used as the fixed centre of symmetry for both polynomial fits. The polynomial parameters $\{a_0, a_2, a_4\}$ are fitted by least squares, in the same way as *Poly4OptCF*, but no iterative root-finding method is required as the centre is already known by Quad.
  Finally, to find the estimated FBG centre frequency, each polynomial curve is intersected with the horizontal line $y = W_{min} + (W_{max} - W_{min})/2$ (centred in the point selection window) and the average of the x-coordinates of the points of intersection (closest to the profile points) is taken as the CF estimate f_c^*. Note that computing intersection point is efficient, as it does not require an iterative numerical method; order-4 polynomial roots are known analytically.
- The *CubicSpline* method: This is similar to the DualPoly4 technique, but it applies cubic spline fitting. It uses piecewise cubic curves that pass through all selected sample points to estimate the profile curves separately on the left and right-hand sides. This method is more computationally intensive but can fit more closely to the sample points. A potential disadvantage is localised overfitting between sample points, increasing the CF estimation error, as demonstrated in following section.

This article has been accepted for publication in Journal of Lightwave Technology. This is the author's version which has not been fully edited and
content may change prior to final publication. Citation information: DOI 10.1109/JLT.2026.3705621

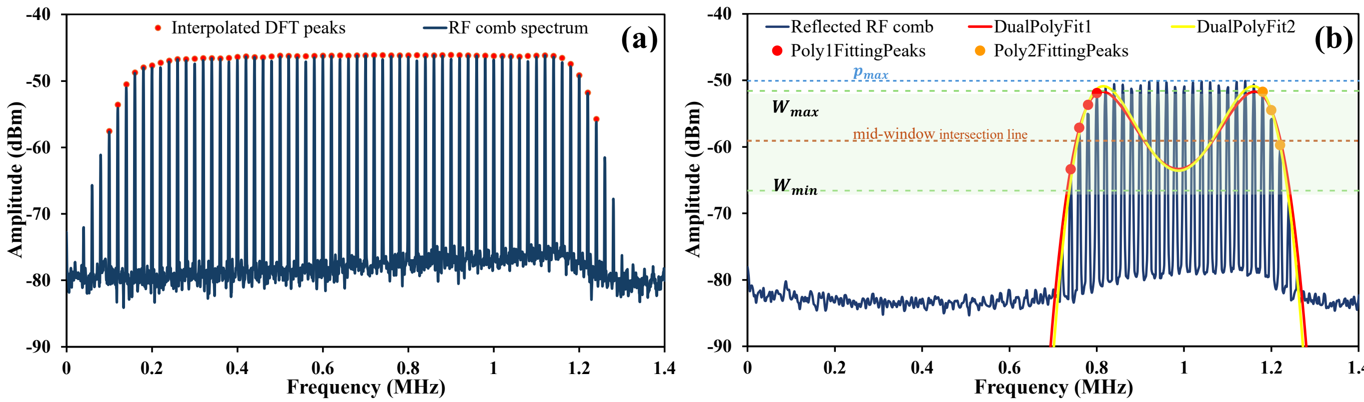

Fig. 6. RF comb spectra **(a)** generated by the DOFC and acquired with a record length of 16,384 samples with a DFT averaging factor of 19 (red markers denote the detected comb line peaks), and **(b)** generated by the DOFC after reflection from the FBG, acquired with a record length of 4,096 samples and a DFT averaging factor of 50. Fitting using the DualPoly4 curve applied.

C. *Simulation and error analysis of curve fitting algorithms*

To estimate worst-case curve fitting systematic error of the proposed curve fitting methods, while excluding other experimental uncertainties (e.g., temperature variations), the following numerical simulation approach was used. The simulations employed a fixed FBG profile, derived from the measured FBG RF spectra. Samples of the FBG peak spectra located at different frequencies (different Bragg wavelengths) were captured using the customised processing platform, as shown in **Fig. 7 (a)**. For simplicity, four of these sample profiles were selected from the entire range. These four samples were aligned in frequency and to the same maximum peak magnitude, after which they were averaged. A high-order polynomial was fitted to the averaged FBG profile points, as depicted in **Fig. 7 (b)**. It can be observed that the left side of the FBG reflection profile exhibits a steeper slope than the right side, indicating that the profile is not perfectly symmetric. This polynomial $p(f - f_c)$ was then used to generate simulated FBG combs, with a 20 kHz line spacing, for any given nominal CF, f_c. The averaged profile was then continuously swept across the RF comb to evaluate the fitting and tracking performance of each method, which is quantified in terms of the CF estimation error and the maximum deviation.

Simulations determine the CF estimation error function, $\varepsilon(f_c)$, where:

$$\varepsilon(f_c) \triangleq f_c - f_c^*.$$

Of particular interest is the maximum deviation in $\varepsilon(f_c)$ over its period,

$$\mathrm{D}\big(\varepsilon(f_c)\big) \triangleq \max\{\varepsilon(f_c)\} - \min\{\varepsilon(f_c)\},\ \ \forall f_c \in [f, f + F_{ls}).$$

Offset in the error function, $\min\{\varepsilon(f_c)\} + \mathrm{D}(\varepsilon(f_c))/2$, is less important as this is constant and can be calibrated out in practice, plus, f_c for an asymmetric profile is arbitrarily defined in any case. An example of the $\varepsilon(f_c)$ function for each of the four methods is shown in **Fig. 7 (c)**, with the maximum deviation $\mathrm{D}(\varepsilon(f_c))$ and offset quoted for each.

The simulation results show that the estimation error, $\varepsilon(f_c)$, is periodic in frequency with a period equal to the RF comb line spacing F_{ls} (20 kHz), which corresponds to a Bragg-wavelength shift of about 8.03 pm. In essence, as the spectral profile shifts relative to the fixed optical-comb lines, the peak selection window periodically gains or loses a pair of comb lines at its edges when the amplitudes of those edge peaks fluctuate. The set of points used for the fitting is then changed. This change alters the fitted envelope and produces a step-like change in the extracted CF.

This simulation, therefore, isolates the intrinsic algorithmic resolution limit imposed by the discrete comb sampling, establishing the minimum achievable interrogation resolution for a given comb line spacing.

Comparative simulation results indicate a clear trade-off among estimator complexity, robustness and accuracy. Table I summarizes the maximum error deviation and the systematic error behaviour observed for the four fitting methods. The symmetric curve fitting methods, *Quad* and *Poly4OptCF*, exhibit larger periodic errors compared to the other approaches, with maximum deviations of 0.977 kHz and 1.346 kHz, respectively. The *DualPoly4* achieved the best overall performance, reducing the periodic CF deviation by approximately an order of magnitude compared with the quadratic baseline reported in [24], while retaining computational efficiency. Its principal vulnerability is degraded performance when low-SNR tail points are included in the fitting window, which can be mitigated via a conservative window selection and post-hoc calibration of constant offsets. The *CubicSpline* yielded competitive accuracy for larger fitting windows but demanded higher computational resources.

The results also confirm that, when the FBG spectral profile is not perfectly symmetric, symmetric curve fitting methods such as *Quad* and *Poly4OptCF* introduce increased systematic errors, whereas *CubicSpline* and *DualPoly4*, which are capable of accommodating various FBG profiles, enable more accurate Bragg wavelength tracking. Therefore, the DualPoly4 fitting algorithm is used in the remaining experiments.

This article has been accepted for publication in Journal of Lightwave Technology. This is the author's version which has not been fully edited and
content may change prior to final publication. Citation information: DOI 10.1109/JLT.2026.3705621

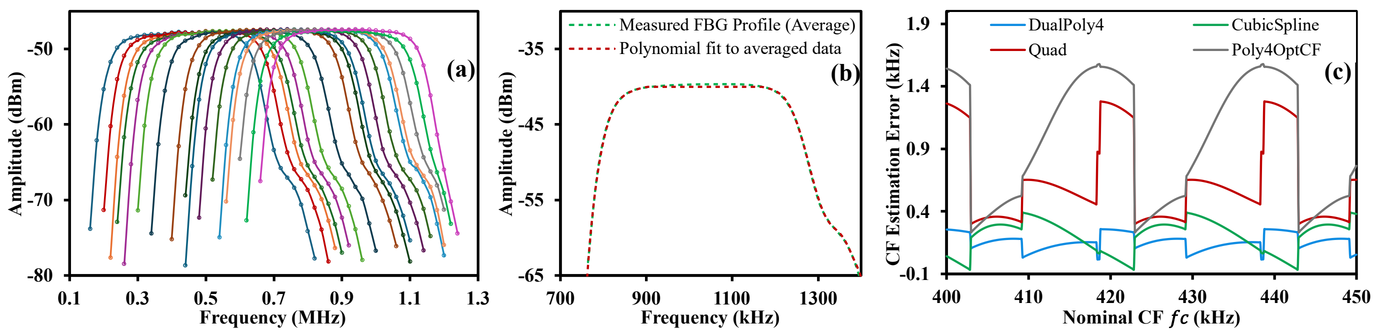

Fig. 7. (a) Captured FBG spectral profiles across a range of Bragg wavelength settings, **(b)** averaged FBG spectra and high order polynomial fit, used as simulated profile, and **(c)** centre frequency estimation error functions for each of the four methods. Simulation settings: $F_{ls} = 20$ kHz, FBG profile: polynomial fit to measured data with max. level shifted to $P_{max} - 40$dBm. $W_{max} = -41$ dBm, $W_{min} = -51$ dBm. Centre frequency sweep from 400 kHz to 450 kHz in increments of 0.12345 kHz.

Table I. Comparison of curve fitting methods: maximum error deviation and estimation error (kHz)

Fitting method	*Quad*	*Poly4OptCF*	*Cubic Spline*	*DualPoly4*
$D(\varepsilon(f_c))$ (kHz)	0.977	1.346	0.457	0.242
$\varepsilon(f_c)$ (kHz)	0.790	0.905	0.162	0.138

A representative example of the DualPoly4 algorithm applied to the RF comb used is shown in **Fig. 6 (b)**. In practice, a configurable peak-selection window first selects the comb lines for fitting: the upper threshold is $W_{max} = p_{max} - 1.5$ (1.5 dB down from the highest peak) and the lower threshold is $W_{min} = W_{max} - 15$ (window width = 15 dB). These parameters are chosen to exclude noisier points further from the maximum peak while retaining the comb lines located on the two slopes of the FBG reflection profile. This reduces the influence of larger amplitude fluctuations associated with low-SNR comb lines, thereby improving the robustness and achievable resolution of the fitting process. In the illustrated example, four left-side peaks (red markers) and three right-side peaks (orange markers) lie inside this window and are treated as two independent subsets. Each symmetric fourth-order polynomial is solved analytically for the intersection points at the mid-window level Y (by reducing the equation to a quadratic in $(x-c)^2$). The estimated CF is the midpoint of the two outermost real roots (one x per side).

V. Analysis of Static Interrogation and Discussion of Experimental Results

Using the optimised DOFC interrogator and the customised real-time processing platform running the DualPoly4 estimator, we performed static interrogations by shifting the FBG to discrete Bragg wavelengths so that the resulting down-converted CFs in the RF domain were 405 kHz, 505 kHz, 605 kHz, 705 kHz, 805 kHz, 905 kHz, and 985 kHz.

For each Bragg wavelength setting, the CF was recorded for 100 seconds using a sample length of 4096 and a DFT averaging factor of 500, yielding a measurement rate of 2.63 CF measurements per second. The standard deviation (σ) of the estimated CF was taken as the measurement resolution. **Fig. 8 (a)** shows the estimated CF for different Bragg wavelength settings. The CF estimates, taken for the chosen wavelength steps, exhibit standard deviations in the order of hundreds of Hz. The largest variation was observed at $CF = 985\ kHz$, where the CF standard deviation was 161.58 Hz, corresponding to a Bragg wavelength interrogation uncertainty of 64.9 fm, calculated as $\lambda_{uncer} = \frac{STDEV_{CF}}{f_{ls}} \times FSR$.

Increasing the DFT averaging factor reduces the influence of high-frequency amplitude fluctuations in the interrogation results, but it also increases data-processing time and therefore lowers the acquisition speed. To demonstrate the relationship between capture rate and measurement resolution, and to evaluate the system's real-time capability, static-interrogation measurements were performed with different averaging settings. For each of the selected CFs, the DFT averaging factor was changed from 1 to 500. For a CF of 985 kHz, the sweep was extended up to 1,320. Under the same CF conditions, three independent tests were recorded for each averaging setting to ensure repeatability. From these measurements, the relationship between the measurement rate and resolution was derived. As the averaging factor increased from 1 to 1,320, the measurement rate decreased from 1011 Hz to 1 Hz. **Fig. 8 (b)** shows the evolution in the standard deviation of the CF with different measurement rates (X-axis) for different values of the CF (different colours). The experiment was designed to demonstrate two key points:

- the relationship between σ and measurement rate
- at a fixed averaging (measurement rate), the relationship between σ and CF.

To ensure a 95% confidence interval corresponding to a relative error below ±5%, a sufficient number of independent samples were collected at each averaging setting. Therefore, for averaging factors from 1 to 700 (measurement rates from 1011 Hz down to 1.88 Hz), the static interrogation duration was set to 100 seconds. For averaging factors above 700 and up to 1,320 (measurement rates from 1.88 Hz to 1 Hz), the static interrogation duration was increased to 200 seconds.

This article has been accepted for publication in Journal of Lightwave Technology. This is the author's version which has not been fully edited and content may change prior to final publication. Citation information: DOI 10.1109/JLT.2026.3705621

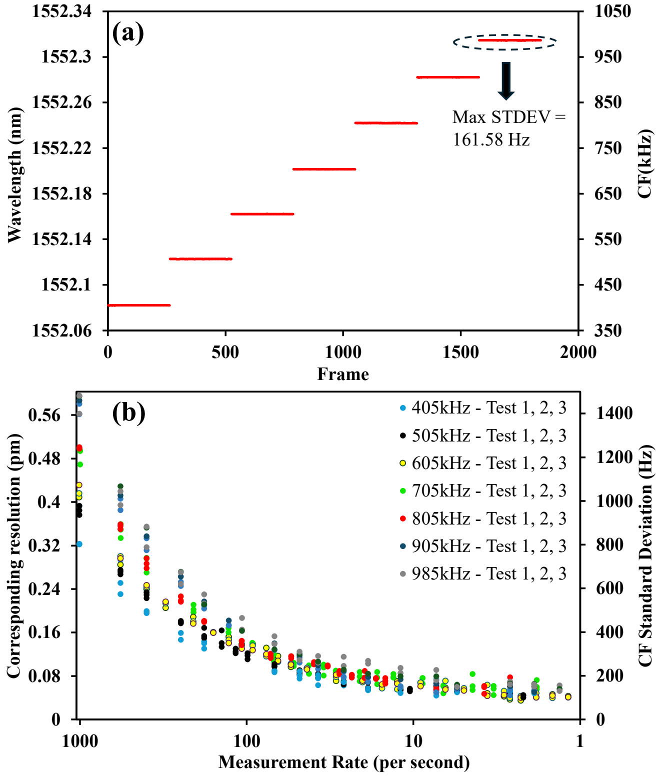

Fig. 8. Static FBG interrogation results **(a)** Estimated CF for different Bragg-wavelength settings, and **(b)** σ of the estimated CF across different Bragg wavelengths and measurement rates.

As shown in **Fig. 8 (b)**, for each Bragg wavelength setting (corresponding to different CFs), the σ of the CF decreased as the measurement rate fell (i.e., as the averaging factor increased). This behaviour indicated that increasing the averaging factor improved the resolution. This effect is expected because increasing the averaging factor filters out high-frequency amplitude fluctuations in the RF comb that would otherwise bias the curve fitting process, thereby yielding higher resolution. In other words, averaging reduces high-frequency noise in the RF-comb envelope, improving the stability of the fitted envelope and the accuracy of the extracted CF.

It is worth noting that, despite efforts to thermally isolate the FBG from the environment, an internal microcontroller within the AOS unit generates heat, and absolute thermal stability during static interrogation cannot be guaranteed. Consequently, three repeated static interrogations were carried out at the same CF, and the averaging factor showed negligible variations in the measured σ. In addition, the longer interrogation durations used for averaging factors above 700 (measurement rate below 1.88 Hz) produce a small step increase in σ. This increase is likely due to greater temperature drift over the extended acquisition period and because the system is operating close to its ultimate resolution limit.

Another notable finding was that at low averaging factors, the σ varied significantly between CFs. For a given measurement rate, σ increased with CF (i.e., as the Bragg wavelength shifted toward longer wavelengths), indicating reduced resolution. For example, at an averaging factor of 1 (measurement rate = 1011 Hz), the CF σ was approximately 800 Hz at 405 kHz, about 1,240 Hz at 805 kHz, and 1,450 Hz at 985 kHz, corresponding to a degradation in static measurement resolution from 321.6 fm to 582.9 fm as the Bragg wavelength shifted to longer values. This behaviour is consistent with the OFC amplitude-stability characteristics discussed in Section III, where increased amplitude fluctuations were observed at longer wavelengths due to reduced comb-line SNR, which in turn degrades the resolution. The effect was most pronounced at low averaging factors (high measurement rate). As the averaging factor increased, these differences diminished. When the averaging factor exceeds 13 (measurement rate below ~99 Hz), the σ difference across CFs fell below 200 Hz. When the averaging factor exceeds 500 (measurement rate below ~2.63 Hz), the σ difference across CFs was less than 100 Hz, and the σ values for all CFs converged to the 80 to 180 Hz range. The lowest observed CF σ, 87.87 Hz (corresponding to 35.33 fm uncertainty), occurred at CF = 605 kHz with an averaging factor of 580 (measurement rate = 2.27 Hz).

Overall, the static FBG interrogation experiments quantitatively demonstrate the performance limits and speed-resolution trade-off of the proposed interrogation system, while also validating the wavelength-dependent resolution behaviour predicted by the OFC amplitude-stability analysis in Section III. Using the optimised DOFC and the embedded real-time receiver, interrogation rates exceeding 1 kHz were achieved, while a minimum static interrogation uncertainty of 35.33 fm was demonstrated at lower measurement rates. These results highlight the capability of the proposed system to deliver both high-speed and high-resolution FBG interrogation within a compact, low-cost, and fully real-time architecture.

VI. Conclusion

A compact and low-cost FBG interrogation system comprising an EI-GSL DOFC interrogator and a purpose-built embedded real-time receiver is presented. A key contribution of this work is the realisation of a real-time receiver, in which data acquisition and signal processing are performed on-board using low-cost embedded hardware. In addition, four curve fitting algorithms are evaluated via simulation, resulting in the selection of the DualPoly4 algorithm as an effective balance between accuracy and computational efficiency. System-level experiments, including OFC stability measurements and static interrogation tests at multiple Bragg wavelengths, revealed a clear wavelength-dependent resolution behaviour caused by comb-line SNR variations. Finally, a clear speed-resolution trade-off was experimentally demonstrated, with measurement rates exceeding 1 kHz achieving a worst-case static resolution of 0.582 pm, while increasing the DFT averaging factor (corresponding to measurement rates below 3 Hz) improved the worst-case resolution to 0.073 pm, with a best measured resolution of 0.036 pm. Although the demonstrated interrogation range is smaller than that of conventional FBG interrogation approaches, such as TL based interrogators that can achieve greater dynamic ranges, these systems typically operate with wavelength resolutions at the pm level. In contrast, the proposed system demonstrates higher achievable resolution while maintaining real-time operation; importantly, the superior wavelength tunability of the EI-GSL based OFC provides clear potential to extend the interrogation range.

References

[1] K. O. Hill *et al.*, 'Photosensitivity in optical fiber waveguides: Application to reflection filter fabrication', *Applied Physics Letters*, vol. 32, no. 10, pp. 647–649, May 1978, doi: 10.1063/1.89881.

[2] A. N. Chryssis *et al.*, 'Detecting hybridization of DNA by highly sensitive evanescent field etched core fiber Bragg grating sensors', *IEEE Journal of Selected Topics in Quantum Electronics*, vol. 11, no. 4, pp. 864–872, Jul. 2005, doi: 10.1109/JSTQE.2005.857724.

[3] G. Hegde *et al.*, 'Fiber Bragg grating sensors for aerospace applications: a review', *ISSS J Micro Smart Syst*, vol. 11, no. 1, pp. 257–275, Jun. 2022, doi: 10.1007/s41683-022-00101-z.

[4] D. Kinet *et al.*, 'Fiber Bragg Grating Sensors toward Structural Health Monitoring in Composite Materials: Challenges and Solutions', *Sensors*, vol. 14, no. 4, Art. no. 4, Apr. 2014, doi: 10.3390/s140407394.

[5] E. De Vita *et al.*, 'A review on radiofrequency, laser, and microwave ablations and their thermal monitoring through fiber Bragg gratings', *iScience*, vol. 26, no. 11, p. 108260, Nov. 2023, doi: 10.1016/j.isci.2023.108260.

[6] M. A. Nagar *et al.*, 'Miniaturized polymer-coated FBGs for high-sensitivity biomedical pressure sensing', *J. Phys. Photonics*, vol. 7, no. 4, p. 045034, Oct. 2025, doi: 10.1088/2515-7647/ae0d3a.

[7] M. A. Nagar *et al.*, 'High-Resolution FBG Strain Sensing With Dual-Comb Interrogation and Optimized Signal Processing', *Journal of Lightwave Technology*, pp. 1–12, 2025, doi: 10.1109/JLT.2025.3567158.

[8] M. M. Werneck *et al.*, 'A Guide to Fiber Bragg Grating Sensors', in *Current Trends in Short- and Long-period Fiber Gratings*, IntechOpen, 2013. doi: 10.5772/54682.

[9] K. O. Hill and G. Meltz, 'Fiber Bragg grating technology fundamentals and overview', *Journal of Lightwave Technology*, vol. 15, no. 8, pp. 1263–1276, Aug. 1997, doi: 10.1109/50.618320.

[10] H. M. Chan *et al.*, 'Continuously Swept Laser Fiber Bragg Grating Data Acquisition System (DAS) Capable of Operating in Extreme Environment', in *2023 International Telemetering Conference*, Las Vegas, NV, USA: International Foundation for Telemetering, Oct. 2023.

[11] Y. Yao *et al.*, 'Performance Optimization Design for a High-Speed Weak FBG Interrogation System Based on DFB Laser', *Sensors*, vol. 17, no. 7, p. 1472, Jul. 2017, doi: 10.3390/s17071472.

[12] Y. Fan *et al.*, 'Ultra-Broadband High-Speed Wavelength-Swept DFB Laser Array and Precision Fiber Bragg Grating Sensor Interrogation System', in *Optical Fiber Communication Conference (OFC) 2025 (2025), paper W3G.3*, Optica Publishing Group, Mar. 2025, p. W3G.3. doi: 10.1364/OFC.2025.W3G.3.

[13] J. Wang *et al.*, 'FPGA-Based Dynamic Wavelength Interrogation System for Thousands of Identical FBG Sensors', *Photonics*, vol. 9, no. 2, p. 79, Jan. 2022, doi: 10.3390/photonics9020079.

[14] D. A. Poiana *et al.*, 'Compact Interrogation System of Fiber Bragg Grating Sensors Based on Multiheterodyne Dispersion Interferometry for Dynamic Strain Measurements', *Sensors*, vol. 22, no. 9, Art. no. 9, Jan. 2022, doi: 10.3390/s22093561.

[15] N. Kuse *et al.*, 'Static FBG strain sensor with high resolution and large dynamic range by dual-comb spectroscopy', *Opt. Express, OE*, vol. 21, no. 9, pp. 11141–11149, May 2013, doi: 10.1364/OE.21.011141.

[16] J. E. Posada-Roman *et al.*, 'Fast Interrogation of Fiber Bragg Gratings with Electro-Optical Dual Optical Frequency Combs', *Sensors*, vol. 16, no. 12, Art. no. 12, Dec. 2016, doi: 10.3390/s16122007.

[17] I. Coddington *et al.*, 'Dual-comb spectroscopy', *Optica, OPTICA*, vol. 3, no. 4, pp. 414–426, Apr. 2016, doi: 10.1364/OPTICA.3.000414.

[18] K. Zhao *et al.*, 'Free-running dual-comb fiber laser mode-locked by nonlinear multimode interference', *Opt. Lett., OL*, vol. 44, no. 17, pp. 4323–4326, Sep. 2019, doi: 10.1364/OL.44.004323.

[19] J. Guo *et al.*, 'Multiplexed static FBG strain sensors by dual-comb spectroscopy with a free running fiber laser', *Opt. Express, OE*, vol. 26, no. 13, pp. 16147–16154, Jun. 2018, doi: 10.1364/OE.26.016147.

[20] E. P. Martin *et al.*, 'Stability Characterisation and Application of Mutually Injection Locked Gain Switched Optical Frequency Combs for Dual Comb Spectroscopy', *J. Lightwave Technol.*, vol. 41, no. 13, pp. 4516–4521, Jul. 2023, doi: 10.1109/JLT.2023.3255550.

[21] C. Quevedo-Galán *et al.*, 'Gain-switched semiconductor lasers with pulsed excitation and optical injection for dual-comb spectroscopy', *Opt. Express, OE*, vol. 28, no. 22, pp. 33307–33317, Oct. 2020, doi: 10.1364/OE.404398.

[22] A. Rosado *et al.*, 'Dual optical frequency comb using a multi-functional PIC based on fully integrated injection locked gain-switched lasers', *Sci Rep*, vol. 16, no. 1, p. 3186, Dec. 2025, doi: 10.1038/s41598-025-33112-5.

[23] M. A. Nagar *et al.*, 'FBG bandwidth impact on dual-comb interrogation for high fidelity strain sensing', *Optics & Laser Technology*, vol. 197, p. 114840, May 2026, doi: 10.1016/j.optlastec.2026.114840.

[24] M. Wei *et al.*, 'Real-time FBG wavelength shift sensing system using a gain switched dual comb', in *2025 50th Optical Fiber Communications Conference and Exhibition (OFC)*, San Francisco, California, USA: OPTICA, Mar. 2025.

[25] X. Zhao *et al.*, 'Dual-Comb Dynamic Interrogation of Fiber Bragg Grating With One Mode-Locked Fiber Laser', *IEEE Sensors Journal*, vol. 18, no. 16, pp. 6621–6626, Aug. 2018, doi: 10.1109/JSEN.2018.2852846.

[26] A. Rosado *et al.*, 'Experimental study of optical frequency comb generation in gain-switched semiconductor lasers', *Optics & Laser Technology*, vol. 108, pp. 542–550, Dec. 2018, doi: 10.1016/j.optlastec.2018.07.038.

[27] G. R. C. Possetti *et al.*, 'Metrological Evaluation of Optical Fiber Grating-Based Sensors: An Approach Towards the Standardization', *Journal of Lightwave Technology*, vol. 30, no. 8, pp. 1042–1052, Apr. 2012, doi: 10.1109/JLT.2011.2167500.

[28] H.-W. Lee *et al.*, 'Accuracy improvement in peak positioning of spectrally distorted fiber Bragg grating sensors by Gaussian curve fitting', *Appl. Opt., AO*, vol. 46, no. 12, pp. 2205–2208, Apr. 2007, doi: 10.1364/AO.46.002205.

[29] P. M. Anandarajah *et al.*, 'Generation of Coherent Multicarrier Signals by Gain Switching of Discrete Mode Lasers', *IEEE Photonics Journal*, vol. 3, no. 1, pp. 112–122, Feb. 2011, doi: 10.1109/JPHOT.2011.2105861.

[30] A. Rosado *et al.*, 'Optical frequency comb generation via pulsed gain-switching in externally-injected semiconductor lasers using step-recovery diodes', *Optics & Laser Technology*, vol. 131, p. 106392, Nov. 2020, doi: 10.1016/j.optlastec.2020.106392.

[31] K. Duda, 'DFT Interpolation Algorithm for Kaiser–Bessel and Dolph–Chebyshev Windows', *IEEE Transactions on Instrumentation and Measurement*, vol. 60, no. 3, pp. 784–790, Mar. 2011, doi: 10.1109/TIM.2010.2046594.

[32] P. Anandarajah *et al.*, 'Self-seeding of a gain-switched integrated dual-laser source for the generation of highly wavelength-tunable picosecond optical pulses', *IEEE Photonics Technology Letters*, vol. 16, no. 2, pp. 629–631, Feb. 2004, doi: 10.1109/LPT.2003.821252.